ORIGINAL ARTICLE

High-order Accurate Beam Models Based on Discontinuous Galerkin Methods

Vincenzo Gulizzi[1] · Ivano Benedetti[1] · Alberto Milazzo[1]

Abstract

A novel high-order accurate approach to the analysis of beam structures with bulk and thin-walled cross-sections is presented. The approach is based on the use of a variable-order polynomial expansion of the displacement field throughout both the beam cross-section and the length of the beam elements. The corresponding weak formulation is derived using the symmetric Interior Penalty discontinuous Galerkin method, whereby the continuity of the solution at the interface between contiguous elements as well as the application of the boundary conditions is weakly enforced by suitably defined boundary terms. The accuracy and the flexibility of the proposed approach are assessed by modeling slender and short beams with standard square cross-sections and airfoil-shaped thin-walled cross-sections subjected to bending, torsional and aerodynamic loads. The comparison between the obtained numerical results and those available in the literature or computed using a standard finite-element method shows that the present method allows recovering three-dimensional distributions of displacement and stress fields using a significantly reduced number of degrees of freedom.

Keywords High-order beam models · Thin-walled structures · Discontinuous Galerkin methods

1 Introduction

Beam structures are widely employed in aeronautical and aerospace engineering as they enable the design of structural components with high-performance load-bearing capabilities, structural stiffness and optimized load distribution. Generally, the geometry of a beam structure is characterized by its length and its cross-section, with the former being significantly larger than the dimensions of the latter.

Owing to their geometric features, the mechanical response of beam structures is typically modeled by the so-called classical beam theories, such as the Euler beam theory (EBT) or the Timoshenko beam theory (TBT), which are based on assuming that the displacement components may have up to a linear dependence on the spatial coordinates spanning the beam cross-section [1]. This hypothesis allows expressing the mechanics of beam structures as a one-dimensional problem, with significant reduction in terms of degrees of freedom with respect to three-dimensional

models. However, although classical beam theories are widely employed in various engineering fields and are found in several finite-element software libraries, they may lose accuracy when the length of the considered beam becomes comparable to the dimensions of the cross-section; in fact, for these cases, the use of three-dimensional solid-mechanics models is often recommended. Additionally, while three-dimensional models directly provide the distribution of all stress components, classical beam theories require a few post-processing steps to recover the transverse stress distribution throughout the cross-section.

To ameliorate these shortcomings, several researchers have proposed to extend classical beam theories by using higher order approximations of the displacement components with respect to the cross-section coordinates. Early examples of higher order beam theories may be found in Refs. [2–4], where the authors proposed a third-order displacement approximation for beams with rectangular cross-sections and were able to recover the quadratic variation of the transverse shear stresses. Additional effects, such as primary and secondary torsional warping, were later addressed by Kim and White [5] and Taufik et al. [6] for composite box beams. In the aforementioned studies, the authors used polynomial expansions throughout the cross-section but

✉ Vincenzo Gulizzi
  vincenzo.gulizzi@unipa.it

1 Department of Engineering, Università degli Studi di Palermo, Palermo, Italy
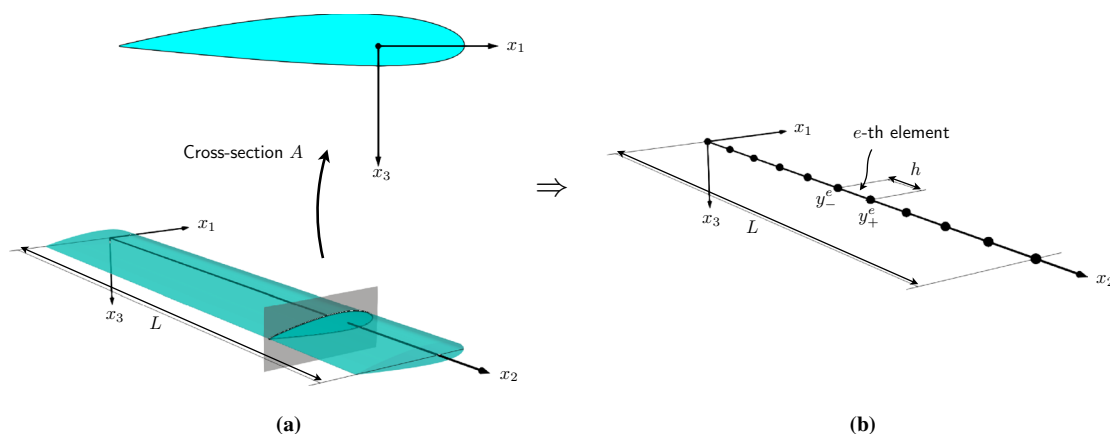
Fig. 1 **a** Three-dimensional beam structure of length L and cross-section A. **b** Discretization of the beam in one-dimensional elements of size h

the use of trigonometric or exponential functions was also investigated by, e.g., Mistou et al. [7] and Karama et al. [8], respectively.

A generalization of these approaches has been proposed by Carrera and co-workers [9, 10], who developed a unified formulation where the order of approximation is a free parameter of the model and allows tuning the accuracy of the solution throughout the beam cross-section. Their approach has been employed to study the static response of laminated composite beams in both the small-strain [11] and large-strain [12–14] regimes, the free-vibration problem of beams with arbitrary cross-sections [15], and the buckling problem of isotropic and composite beams [16]. Recently, high-order theories have also been coupled to fluid dynamics using the Vortex Lattice Method [17] and a finite-volume-based computational fluid-dynamics library [18].

The solution of the equations governing the mechanical response of classical or higher order beam theories is generally obtained via numerical methods since analytical solutions exist for special cases of boundary conditions and/or material properties. The most employed numerical technique for modeling beams, and, more generally, solid mechanics problems, is the finite element method (FEM). The literature offers many examples of FEM-based solutions of beam structures modeled by higher order theories; very recent contributions include the development of finite-element models for large-strain [19], free-vibration and buckling [20, 21], thermo-mechanical coupling [22], non-linear dynamics [23] and wave-propagation [24, 25] problems, among others.

Alternatives to FEM have also been proposed to improve the flexibility and the performance of numerical methods. Among these, the discontinuous Galerkin (DG) method [26] has proved a powerful technique that, being based on

a discontinuous approximations of the solution among the mesh elements, naturally enables the use of different basis functions for different elements of the same mesh, variable-order accuracy and ease of parallelization.

In the literature, a few examples of DG methods applied to the analysis of beam structures are available; these are typically limited to classical beam theories: Celiker et al. [27, 28] developed a DG-based solution of the Timoshenko beam problem and showed that their approach does not suffer from shear locking effects; Eptaimeros et al. [29] developed an Interior Penalty DG methods for Euler beams obeying gradient elasticity; Becker and Noels [30] exploited the discontinuous nature of DG methods to introduce suitably-defined cohesive laws at the interface between contiguous elements of beam structured modeled by the classical EBT. On the other hand, while DG methods have been proposed for the analysis of multilayered structures modeled by higher-order structural theories in the context of small-strain [31–35], large-strain [36] and buckling [37] problems, DG methods for higher-order beam theories have not been investigated. Therefore, in this contribution, Interior Penalty DG methods for the solution of the equations governing the static response of beams modeled by higher order theories are developed and numerically tested.

The remainder of the paper is organized as follows: Sect. 2 introduces the problem statement for the static analysis of beam structures modeled by variable-order beam theories; Sect. 3 presents the solution of the considered problem based on a novel DG formulation; in Sect. 4, the numerical performance of the proposed approach is assessed by considering the response of a beam with a bulk square cross-section to bending and torsional loads, and the response of a beam with thin-walled airfoil-shaped cross-section subjected to bending and aerodynamic loads. Eventually, Sect. 5 draws the conclusions.

2 Problem Statement

We consider a beam with length L and cross-section A as sketched in Fig. 1a. The beam is referred to a global reference system $Ox_1x_2x_3$ located at one end of the beam such that the coordinates x_1 and x_3 span the cross-section A, the coordinate x_2 spans the length of the beam, and the volume V of the beam is identified by $V \equiv [0, L] \times A$. Eventually, the boundary of the beam is denoted by S.

The following mechanical fields are introduced: the displacement field, denoted by the vector $\boldsymbol{u} \equiv (u_1, u_2, u_3)^\mathsf{T}$, and the strain and stress fields that, using Voigt notation, are described by the vectors $\boldsymbol{\gamma} \equiv (\gamma_{11}, \gamma_{22}, \gamma_{33}, \gamma_{23}, \gamma_{13}, \gamma_{12})^\mathsf{T}$ and $\boldsymbol{\sigma} \equiv (\sigma_{11}, \sigma_{22}, \sigma_{33}, \sigma_{23}, \sigma_{13}, \sigma_{12})^\mathsf{T}$, respectively.

In the following, the Einstein summation convention is used with Latin subscripts taking values in $\{1, 2, 3\}$ and Greek subscripts taking values in $\{1, 3\}$.

2.1 Strain–Displacement Relationship

The beam is assumed to undergo small deformations. Following Refs. [31, 32], this allows expressing the vector $\boldsymbol{\gamma}$ containing the strain components as a function of the displacement field $\boldsymbol{u}$ as follows

$$\boldsymbol{\gamma} = \boldsymbol{I}_k \frac{\partial \boldsymbol{u}}{\partial x_k}, \tag{1}$$

where the matrices $\boldsymbol{I}_1$, $\boldsymbol{I}_2$ and $\boldsymbol{I}_3$ are defined as

$$\boldsymbol{I}_1 \equiv \begin{bmatrix} 1 & 0 & 0 \\ 0 & 0 & 0 \\ 0 & 0 & 0 \\ 0 & 0 & 0 \\ 0 & 0 & 1 \\ 0 & 1 & 0 \end{bmatrix}, \quad \boldsymbol{I}_2 \equiv \begin{bmatrix} 0 & 0 & 0 \\ 0 & 1 & 0 \\ 0 & 0 & 0 \\ 0 & 0 & 1 \\ 0 & 0 & 0 \\ 1 & 0 & 0 \end{bmatrix} \quad \text{and} \quad \boldsymbol{I}_3 \equiv \begin{bmatrix} 0 & 0 & 0 \\ 0 & 0 & 0 \\ 0 & 0 & 1 \\ 0 & 1 & 0 \\ 1 & 0 & 0 \\ 0 & 0 & 0 \end{bmatrix}. \tag{2}$$

If one separates the derivatives with respect to x_2 from the derivatives with respect to x_1 and x_3, the vector $\boldsymbol{\gamma}$ may also be written as

$$\boldsymbol{\gamma} = \boldsymbol{I}_2 \frac{\partial \boldsymbol{u}}{\partial x_2} + \boldsymbol{I}_\alpha \frac{\partial \boldsymbol{u}}{\partial x_\alpha}. \tag{3}$$

2.2 Constitutive Behavior

The beam is assumed homogeneous and linear elastic such that the vector $\boldsymbol{\sigma}$ is related to the vector $\boldsymbol{\gamma}$

$$\boldsymbol{\sigma} = \boldsymbol{C}\,\boldsymbol{\gamma}, \tag{4}$$

where the matrix $\boldsymbol{C}$ contains the elastic stiffness coefficients. For the explicit expression of the components of $\boldsymbol{C}$

for isotropic, orthotropic and generally anisotropic elastic materials the reader is referred to Ref. [38].

2.3 High-order Beam Theories

In the context of high-order beam theories, see, e.g., Refs. [10], the k-th displacement component u_k is expressed as a series of products between functions of the cross-section coordinates x_1 and x_3 and functions of the beam length coordinate x_2 playing the role of generalized displacements, that is

$$u_k = \sum_{n=0}^{N_{u_k}} Z^{(kn)}(x_1, x_3) U^{(kn)}(x_2). \tag{5}$$

In Eq. (5), $Z^{(kn)}(x_1, x_3)$ and $U^{(kn)}(x_2)$ represent the generic n-th cross-section function and the n-th generalized displacement for the k-th component of displacement; eventually, N_{u_k} denotes the corresponding order of the expansion. The expression given in Eq. (5) may be written in compact form as

$$\boldsymbol{u} = \boldsymbol{Z}(x_1, x_3)\boldsymbol{U}(x_2), \tag{6}$$

where $\boldsymbol{Z}(x_1, x_3)$ is a $3 \times (N_{u_1} + N_{u_2} + N_{u_3} + 3)$ matrix suitably collecting the cross-section functions and $\boldsymbol{U}$ is a $(N_{u_1} + N_{u_2} + N_{u_3} + 3)$ vector collecting the corresponding generalized displacements. To provide an example, using Eq. (6), the Timoshenko beam theory is obtained upon choosing

$$\boldsymbol{Z} \equiv \begin{bmatrix} 1 & 0 & 0 & 0 & 0 \\ 0 & 1 & 0 & x_1 & -x_3 \\ 0 & 0 & 1 & 0 & 0 \end{bmatrix}, \quad \text{and} \quad \boldsymbol{U} \equiv \begin{pmatrix} u & v & w & \theta_z & \theta_x \end{pmatrix}^\mathsf{T}, \tag{7}$$

where $(u, v, w)^\mathsf{T}$ represents the translations of the cross section, while θ_z and θ_x denote its rotations with respect to the x_3 axis and the x_2 axis, respectively. It is worth noting that additional effects, such as the torsion of the beam, may be included by enriching the set of cross-section functions contained in $\boldsymbol{Z}$.

Using Eq.(6) into Eq. (3) and Eq. (4), one obtains the expression of the strain components and stress components, respectively, as functions of the generalized displacements

$$\boldsymbol{\gamma} = \boldsymbol{I}_2 \boldsymbol{Z} \frac{\mathrm{d}\boldsymbol{U}}{\mathrm{d}x_2} + \boldsymbol{I}_\alpha \frac{\partial \boldsymbol{Z}}{\partial x_\alpha} \boldsymbol{U} \quad \text{and} \quad \boldsymbol{\sigma} = \boldsymbol{C} \left(\boldsymbol{I}_2 \boldsymbol{Z} \frac{\mathrm{d}\boldsymbol{U}}{\mathrm{d}x_2} + \boldsymbol{I}_\alpha \frac{\partial \boldsymbol{Z}}{\partial x_\alpha} \boldsymbol{U} \right). \tag{8}$$

2.4 Governing Equations

The governing equations of the beam theories introduced in Sect. 2.3 are derived by means of the Principle of Virtual

Displacements (PVD), which, for the considered beam, reads

$$\int_V \delta\boldsymbol{\gamma}^\intercal \boldsymbol{\sigma}\, \mathrm{d}V = \int_V \delta\boldsymbol{u}^\intercal \overline{\boldsymbol{b}}\, \mathrm{d}V + \int_S \delta\boldsymbol{u}^\intercal \overline{\boldsymbol{t}}\, \mathrm{d}S, \tag{9}$$

where $\delta(\bullet)$ denotes the variation of $(\bullet)$, while $\overline{\boldsymbol{b}} \equiv (\overline{b}_1, \overline{b}_2, \overline{b}_3)^\intercal$ represents the body forces acting on the volume V of the beam and $\overline{\boldsymbol{t}} \equiv (\overline{t}_1, \overline{t}_2, \overline{t}_3)^\intercal$ represents the traction field acting on its surface S.

Upon substituting the expression of $\boldsymbol{\gamma}$ and $\boldsymbol{\sigma}$ given in Eq. (8) into Eq. (9) and integrating throughout the cross-section A, the expression of the PVD for the considered beam theory is obtained:

$$\int_{\mathcal{D}} \left[\frac{\mathrm{d}\delta\boldsymbol{U}^\intercal}{\mathrm{d}x_2}\left(\boldsymbol{Q}\frac{\mathrm{d}\boldsymbol{U}}{\mathrm{d}x_2} + \boldsymbol{R}\,\boldsymbol{U}\right) + \delta\boldsymbol{U}^\intercal\left(\boldsymbol{R}^\intercal\frac{\mathrm{d}\boldsymbol{U}}{\mathrm{d}x_2} + \boldsymbol{S}\,\boldsymbol{U}\right) \right]\mathrm{d}x_2$$
$$= \int_{\mathcal{D}} \delta\boldsymbol{U}^\intercal\overline{\boldsymbol{B}}\, \mathrm{d}x_2 + \delta\boldsymbol{U}^\intercal\overline{\boldsymbol{T}}_0 + \delta\boldsymbol{U}^\intercal\overline{\boldsymbol{T}}_L, \tag{10}$$

where $\mathcal{D} \equiv [0, L]$ is the modeling domain of the beam, $\boldsymbol{Q}$, $\boldsymbol{R}$, $\boldsymbol{S}$ are the generalized stiffness matrices, $\overline{\boldsymbol{B}}$ is the generalized domain load, and $\overline{\boldsymbol{T}}_0$ and $\overline{\boldsymbol{T}}_L$ are the generalized forces at the ends of the beam. Their expression are given as follows. The generalized stiffness matrices are defined as

$$\boldsymbol{Q} \equiv \int_A \boldsymbol{Z}^\intercal \boldsymbol{c}_{22}\boldsymbol{Z}\, \mathrm{d}A, \quad \boldsymbol{R} \equiv \int_A \boldsymbol{Z}^\intercal \boldsymbol{c}_{2\alpha}\frac{\partial\boldsymbol{Z}}{\partial x_\alpha}\, \mathrm{d}A,$$
$$\text{and} \quad \boldsymbol{S} \equiv \int_A \frac{\partial\boldsymbol{Z}^\intercal}{\partial x_\alpha}\boldsymbol{c}_{\alpha\beta}\frac{\partial\boldsymbol{Z}}{\partial x_\beta}\, \mathrm{d}A, \tag{11}$$

where $\boldsymbol{c}_{kl} \equiv \boldsymbol{I}_k^\intercal \boldsymbol{C}\boldsymbol{I}_l$, with $k, l = 1, 2, 3$, are 3×3 matrices collecting subsets of the elastic coefficients of $\boldsymbol{C}$, see, e.g., Ref. [32]. The generalized domain load stems from the body forces $\overline{\boldsymbol{b}}$ and the surface traction acting on the lateral surface of the beam as

$$\overline{\boldsymbol{B}} \equiv \int_A \boldsymbol{Z}^\intercal\overline{\boldsymbol{b}}\, \mathrm{d}A + \int_{\partial A} \boldsymbol{Z}^\intercal\overline{\boldsymbol{t}}\, \mathrm{d}\partial A, \tag{12}$$

where ∂A denotes the contour of the cross-section of the beam. Eventually, the generalized forces associated with the surface traction acting on the beam ends surfaces are defined as

$$\overline{\boldsymbol{T}}_y \equiv \int_A \boldsymbol{Z}^\intercal\overline{\boldsymbol{t}}\Big|_{x_2=y}\, \mathrm{d}A, \quad \text{at} \quad y = 0, L. \tag{13}$$

Finally, by performing integration by parts in Eq. (10) and recalling that the variational statement must be valid for any $\delta\boldsymbol{U}$, one obtains the following strong form of the governing equations

$$-\frac{\mathrm{d}}{\mathrm{d}x_2}\left(\boldsymbol{Q}\frac{\mathrm{d}\boldsymbol{U}}{\mathrm{d}x_2} + \boldsymbol{R}\,\boldsymbol{U}\right) + \boldsymbol{R}^\intercal\frac{\mathrm{d}\boldsymbol{U}}{\mathrm{d}x_2} + \boldsymbol{S}\,\boldsymbol{U} = \overline{\boldsymbol{B}} \quad \text{for } x_2 \in \mathcal{D}. \tag{14}$$

The governing equations given in Eq. (14) are supplemented by suitable boundary conditions, which are enforced at the ends of the beam, i.e., at $x_2 = y$, where $y = 0$ or $y = L$. Dirichlet-type boundary conditions read

$$\boldsymbol{U}|_{x_2=y} = \overline{\boldsymbol{U}}_y \tag{15}$$

where $\overline{\boldsymbol{U}}_y$ is the vector of prescribed generalized displacements at $x_2 = y$; on the other hand, Neumann-type boundary conditions are

$$\nu_y\left(\boldsymbol{Q}\frac{\mathrm{d}\boldsymbol{U}}{\mathrm{d}x_2} + \boldsymbol{R}\,\boldsymbol{U}\right) = \overline{\boldsymbol{T}}_y \tag{16}$$

where $\nu_0 = -1$ and $\nu_L = 1$. It is worth noting that either Dirichlet boundary conditions or Neumann boundary conditions may be enforced at each end of the beam.

3 Discontinuous Galerkin Formulation

The set of governing equations for high-order beam theories introduced in the preceding section, namely Eqs. (14)–(16), is a set of second-order elliptic differential equations with associated boundary conditions. In this section, the corresponding weak form is derived following the Interior Penalty discontinuous Galerkin formulation developed in Refs. [31, 32].

The modeling domain of the beam is divided into N_e non-overlapping elements such that the domain $\mathcal{D}^e$ of the generic e-th element is identified by the interval $\mathcal{D}^e \equiv [y_-^e, y_+^e]$, where y_-^e and y_+^e represent the two ends of the same element. It is clear that $y_+^e \equiv y_-^{e+1}$ and, if the elements have the same size h, $y_-^e = (e-1)h$ and $y_+^e = eh$. The collection of all the elements defines the mesh of the beam, whose discretized domain is denoted by $\mathcal{D}^h \equiv \bigcup_{e=1}^{N_e} \mathcal{D}^e$. The discretization also introduces the set $\mathcal{I}^h$ of the inter-elements interfaces, which collects the boundary points between adjacent elements, i.e. $\mathcal{I}^h \equiv \{y_+^i\}$ with $i = 1, \ldots, N_e - 1$. Eventually, the ends of the beam, namely the points $x_2 = 0$ and $x_2 = L$, are collected into the set $\mathcal{B}_D$ of Dirichlet boundary conditions points or into the set $\mathcal{B}_N$ of Neumann boundary conditions points based on which types of boundary conditions are enforced at these boundary points. For instance, in Sect. 4, the numerical results will be focused on cantilever beams, which means that $\mathcal{B}_D = \{0\}$ and $\mathcal{B}_N = \{L\}$. A sample mesh of the beam of Fig. 1a is shown in Fig. 1b.

Once the mesh has been defined, the approximation of the solution over each element needs to be introduced.

The typical feature of DG formulations is the use of discontinuous basis functions over the mesh. In general, this would allow selecting different spaces of basis functions for different elements of the same mesh, which in turn would enable different *hp*-refinement strategies to improve

The first row and the second row of Eq. (18) are then multiplied by V^T and Γ^T, respectively, where V and Γ are test functions taken from the space $(\mathcal{V}^{hp})^{N_U}$ of discontinuous vector fields, i.e. $V, \Gamma \in (\mathcal{V}^{hp})^{N_U}$. Upon integrating over the generic *e*-th element and using integration by parts, Eq. (18) is stated in weak sense as follows

$$\begin{cases} \int_{\mathcal{D}^e} \left[\frac{\mathrm{d}V^\mathsf{T}}{\mathrm{d}x_2}\Sigma^e + V^\mathsf{T}\left(R^\mathsf{T}\frac{\mathrm{d}U^e}{\mathrm{d}x_2} + S\,U^e \right) \right]\mathrm{d}x_2 = \int_{\mathcal{D}^e} V^\mathsf{T}\overline{B}\,\mathrm{d}x_2 + \sum_{y\in\mathcal{B}^e} V^\mathsf{T}\widehat{\Sigma}\nu_y \\ \int_{\mathcal{D}^e} \Gamma^\mathsf{T}\Sigma^e\,\mathrm{d}x_2 = \int_{\mathcal{D}^e} \Gamma^\mathsf{T}(Q\frac{\mathrm{d}U^e}{\mathrm{d}x_2} + R\,U^e)\mathrm{d}x_2 + \sum_{y\in\mathcal{B}^e}(\Gamma^\mathsf{T}Q + V^\mathsf{T}R^\mathsf{T})(\widehat{U} - U^e)\nu_y \end{cases} \tag{19}$$

the numerical solution, see, e.g., Ref. [39, 40]. However, these aspects are outside the scope of the present research study and the same space of discontinuous polynomials is considered for all the mesh elements. In particular, let us introduce the space $\mathcal{V}^{hp}$ of discontinuous polynomials defined as

$$\mathcal{V}^{hp} \equiv \{v : \mathcal{D}^h \to \mathbb{R} \mid v(x_2 \in \mathcal{D}^e) \in \mathcal{P}^p(\mathcal{D}^e)\ \forall e = 1, \dots, N_e\}, \tag{17}$$

where $\mathcal{P}^p(\mathcal{D}^e)$ is the space of polynomials of degree p defined over the element $\mathcal{D}^e$. Then, the approximate solution U^h of Eqs. (14)–(16) is sought within the space $(\mathcal{V}^{hp})^{N_U}$ of discontinuous vector fields, where N_U is the number of generalized displacements introduced by the considered beam theory.

To obtain the DG-based weak form of Eqs. (14)–(16), Eq. (14) is first rewritten as the following equivalent first-order set of differential equations

$$\begin{cases} -\frac{\mathrm{d}\Sigma}{\mathrm{d}x_2} + R^\mathsf{T}\frac{\mathrm{d}U}{\mathrm{d}x_2} + S\,U = \overline{B} \\ \Sigma = Q\frac{\mathrm{d}U}{\mathrm{d}x_2} + R\,U \end{cases} \tag{18}$$

where: the terms U^e and Σ^e denote the approximate solution of U and Σ over the element e; $\mathcal{B}^e \equiv \{y^e_-, y^e_+\}$; ν_y denotes the unit normal at the element's boundary points, which, being the beam model one dimensional, has values $\nu_{y^e_-} = -1$ and $\nu_{y^e_+} = 1$; and $\widehat{U}$ and $\widehat{\Sigma}$ are the so-called *numerical fluxes* [26], which represent approximate expressions of U and Σ at the elements boundaries.

The numerical fluxes are the characteristic ingredients of DG formulations because they are responsible for linking adjacent elements. In general, at the *i*-th interface between two contiguous elements e and $e + 1$, $\widehat{U}$ and $\widehat{\Sigma}$ are functions of U^e, Σ^e, U^{e+1} and Σ^{e+1}. Their explicit expression depend on the considered DG method: here, upon introducing the approximate solution U^h such that $U^h(x_2 \in \mathcal{D}^e) \equiv U^e$, the numerical fluxes are chosen according to the symmetric Interior Penalty DG formulation developed in Refs. [31, 32] as follows
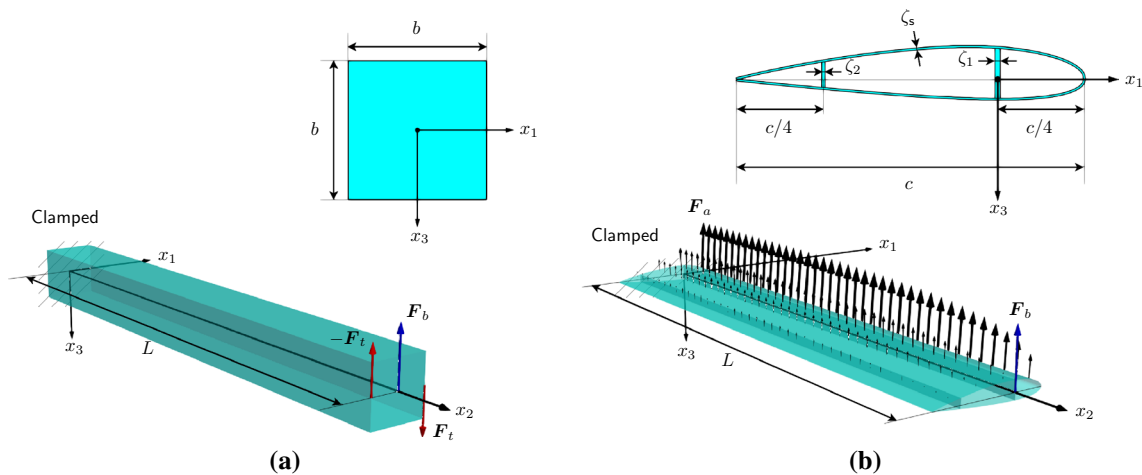

Fig. 2 Geometry, boundary conditions and loads for **a** a beam with a square cross-section and **b** a beam with an airfoil cross-section
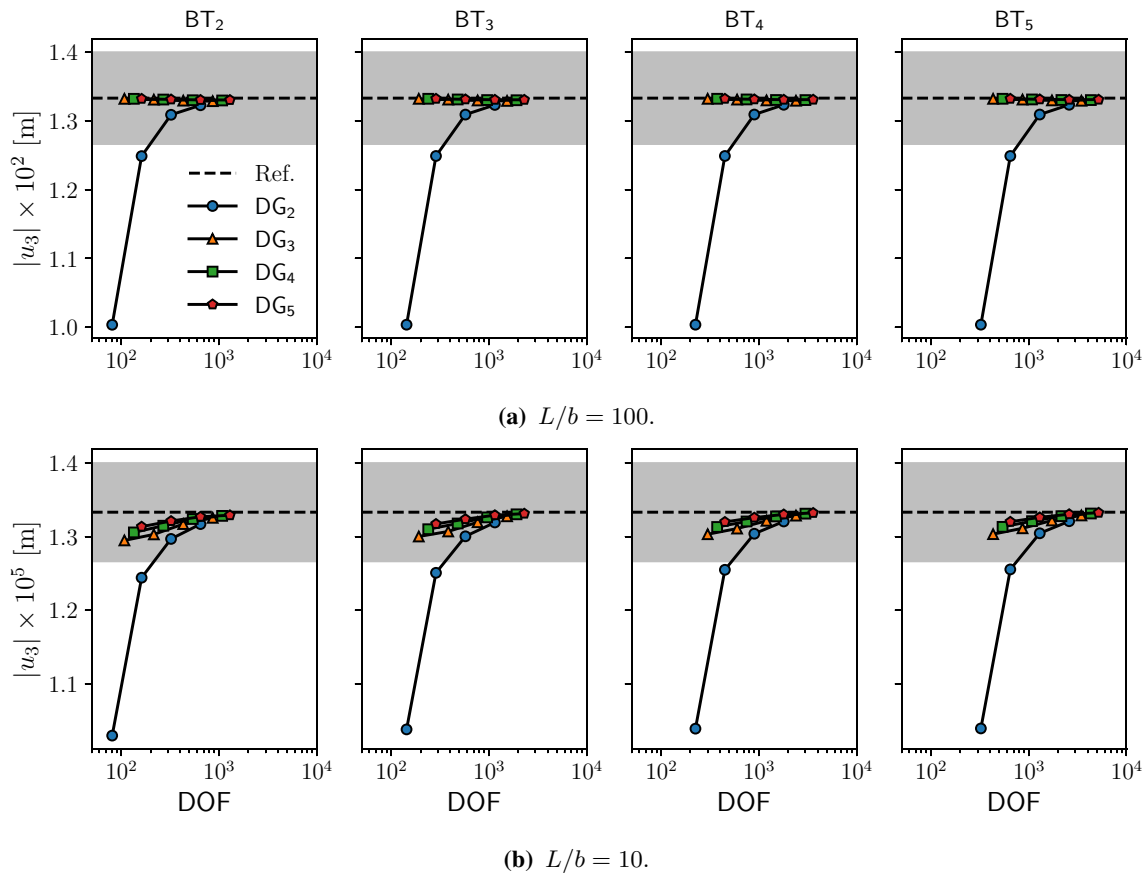
(a) $L/b = 100$.

(b) $L/b = 10$.

Fig. 3 Magnitude of the displacement u_3 at $\boldsymbol{x} = (0, L, 0)^\intercal$ for the beam with the square cross-section subjected to bending as a function of the selected beam theory, polynomial degree and total degrees of freedom. Reference values (the thick dashed lines) are taken from Ref. [9] while the gray area denotes the region of less than 5% deviation from the dashed line

$$
\widehat{\boldsymbol{U}} = \begin{cases} \{\boldsymbol{U}^h\}, & \text{at } x_2 = y \in \mathcal{I}^h \\ \overline{\boldsymbol{U}}_y, & \text{at } x_2 = y \in \mathcal{B}_D \\ \boldsymbol{U}^e, & \text{at } x_2 = y \in \mathcal{B}_N \end{cases}
$$

$$
\text{and} \quad \begin{cases} \widehat{\boldsymbol{\Sigma}} = \left\{ \boldsymbol{Q}\dfrac{\mathrm{d}\boldsymbol{U}^h}{\mathrm{d}x_2} + \boldsymbol{R}\,\boldsymbol{U}^h \right\} - \mu[\![\boldsymbol{U}^h]\!], & \text{at } x_2 = y \in \mathcal{I}^h \\ \widehat{\boldsymbol{\Sigma}} = \boldsymbol{Q}\dfrac{\mathrm{d}\boldsymbol{U}^e}{\mathrm{d}x_2} + \boldsymbol{R}\,\boldsymbol{U}^e - \mu(\boldsymbol{U}^e - \overline{\boldsymbol{U}}_y), & \text{at } x_2 = y \in \mathcal{B}_D \\ \widehat{\boldsymbol{\Sigma}}\nu_y = \overline{\boldsymbol{T}}_y, & \text{at } x_2 = y \in \mathcal{B}_N \end{cases}
$$

(20)

where $\{\bullet\}$ and $[\![\bullet]\!]$ are the *average operator* and *jump operator*, respectively, that are defined at the i-th interface between the elements e and $e + 1$ as

$$
\{\bullet\} \equiv \frac{1}{2}(\bullet^e + \bullet^{e+1}) \quad \text{and} \quad [\![\bullet]\!] \equiv \bullet^e - \bullet^{e+1} \tag{21}
$$

respectively. Additionally, in Eq. (20), μ is the so-called *penalty parameter* that must be suitably chosen. As customary in Interior Penalty DG formulations, see, e.g., Ref. [26], and

consistently with the numerical tests performed in Refs. [31, 32], the penalty parameter μ appearing in Eq. (20) is chosen as $\mu \sim Q/h$, where Q is a positive constant of one or two orders of magnitude larger than the terms in the generalized matrix $\boldsymbol{Q}$ and h is the mesh size.

The interested reader is referred to Ref. [26] for a thorough analysis regarding the effect of different numerical fluxes and the choice of the penalty parameter on the properties of the corresponding DG methods.

As the last step, using Eq. (20) into Eq. (19), setting $\boldsymbol{\Gamma} \equiv \mathrm{d}\boldsymbol{V}/\mathrm{d}x_2$ and summing over all the mesh elements, the weak form of symmetric Interior Penalty DG methods for high-order beam theories considered in this paper is expressed as follows: find $\boldsymbol{U}^h \in (\mathcal{V}^{hp})^{N_U}$ such that

$$
B_{\mathrm{IP}}(\boldsymbol{V}, \boldsymbol{U}^h) = L_{\mathrm{IP}}(\boldsymbol{V}, \overline{\boldsymbol{B}}, \overline{\boldsymbol{T}}, \overline{\boldsymbol{U}}) \tag{22}
$$

for any $\boldsymbol{V} \in (\mathcal{V}^{hp})^{N_U}$. In Eq. (22), the bilinear form $B_{\mathrm{IP}}(\boldsymbol{V}, \boldsymbol{U}^h)$ is defined as
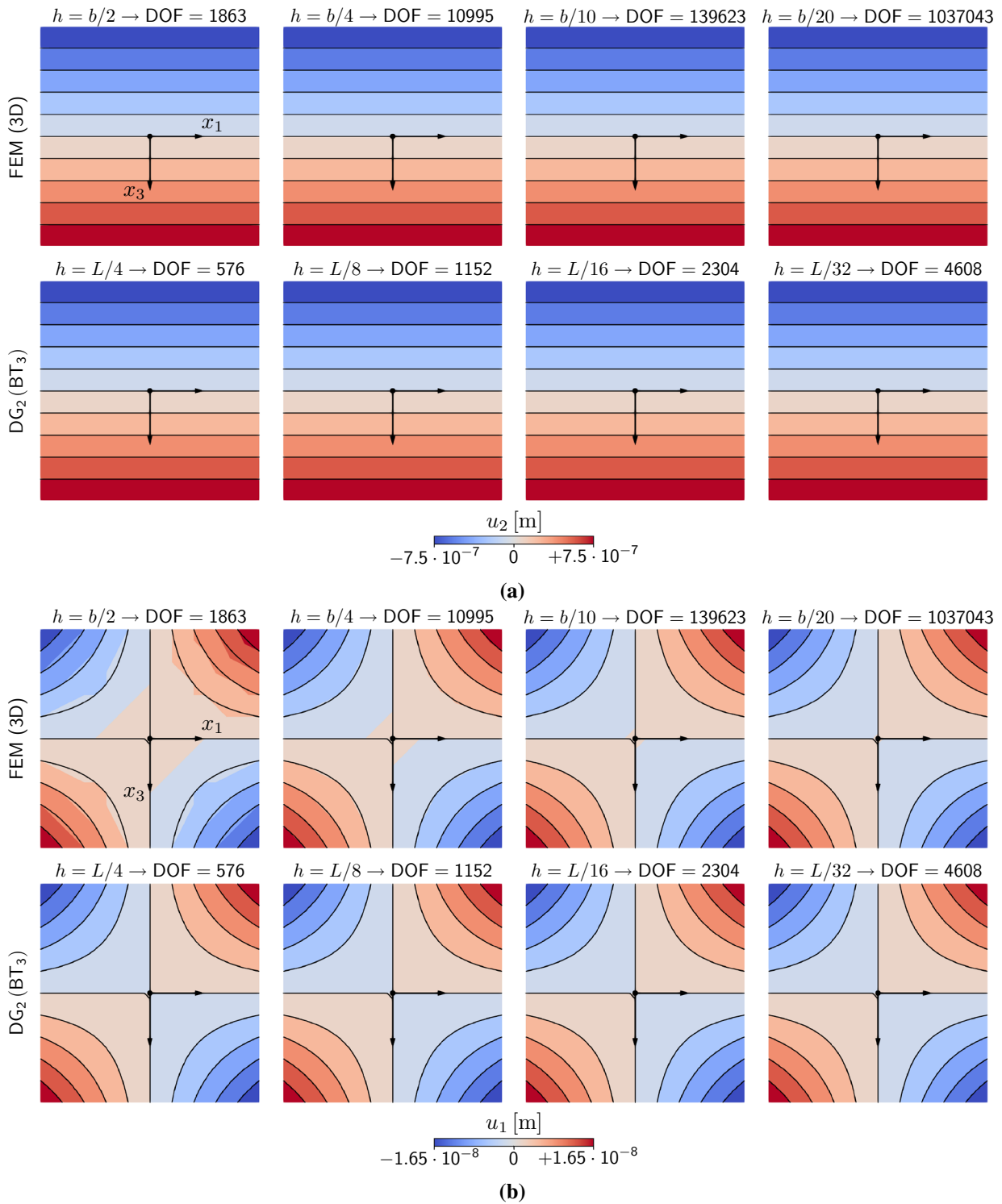
Fig. 4 Comparison between the solution obtained via a 3D FEM model and the proposed DG formulation: effect of the mesh size on the cross-section distribution of **a** the displacement component u_2 and **b** the displacement component u_1 for the short beam subjected to bending
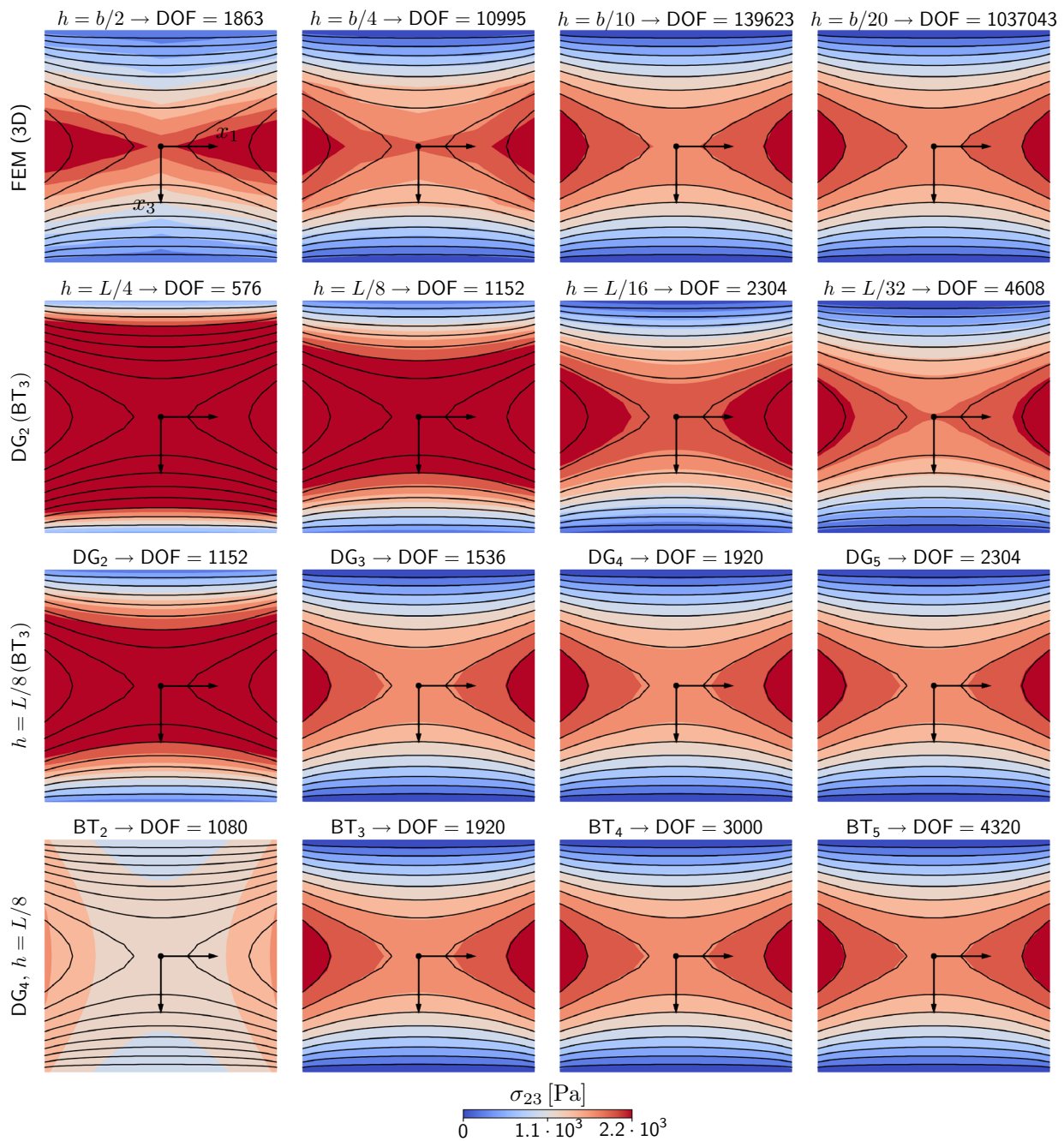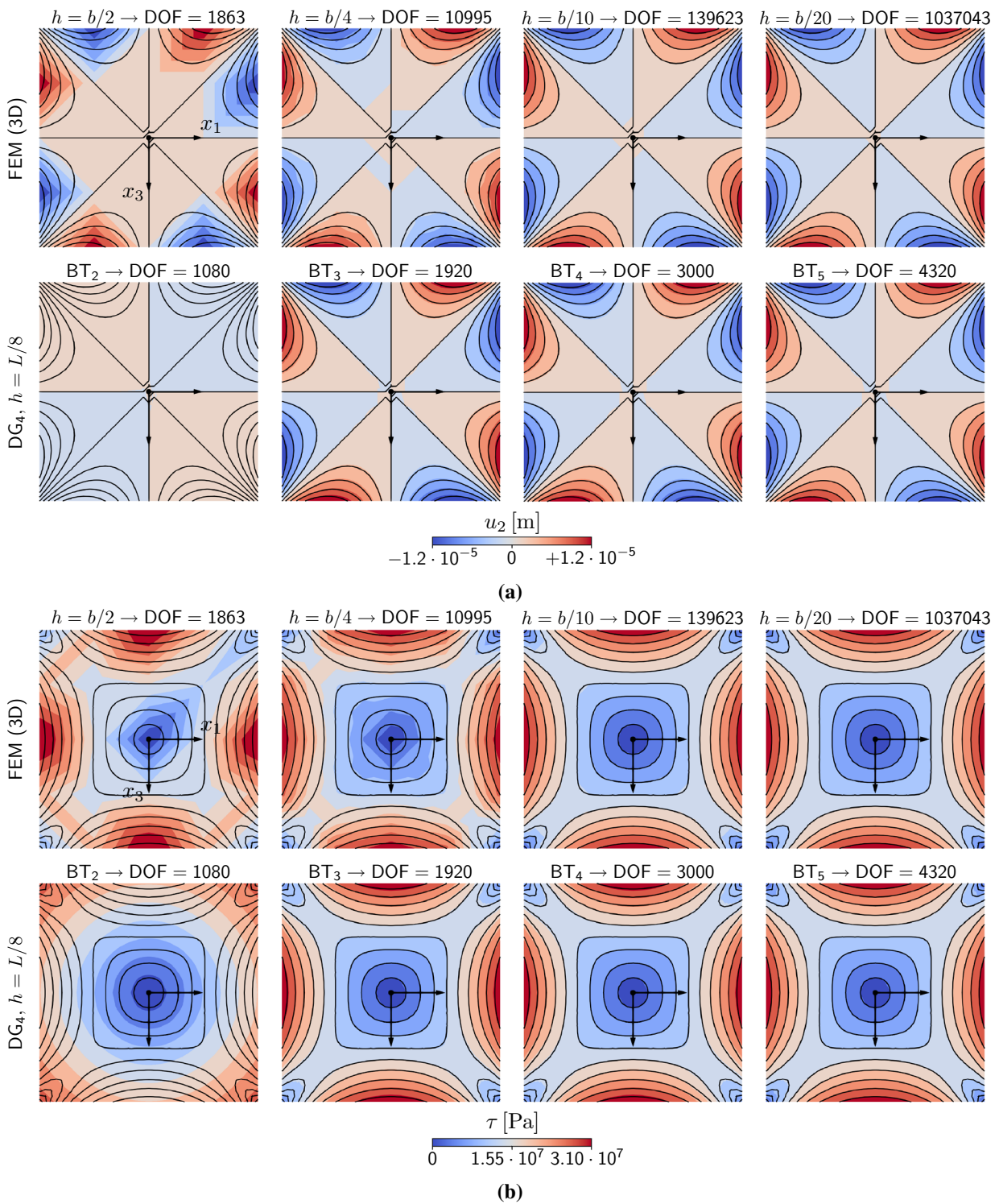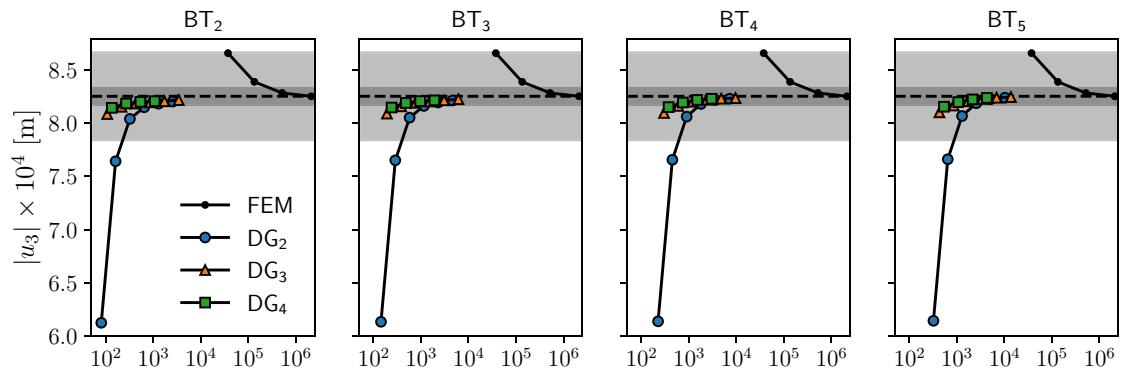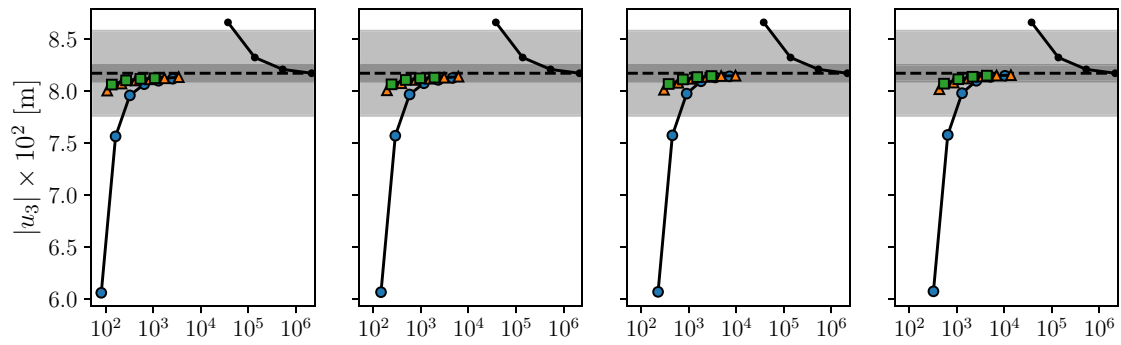
Fig. 5 Comparison between the solution obtained via a 3D FEM model and the proposed DG formulation: the effect of the mesh size, order of the DG basis functions and order the beam theory on the cross-section distribution of the stress component σ_{23} for the short beam subjected to bending
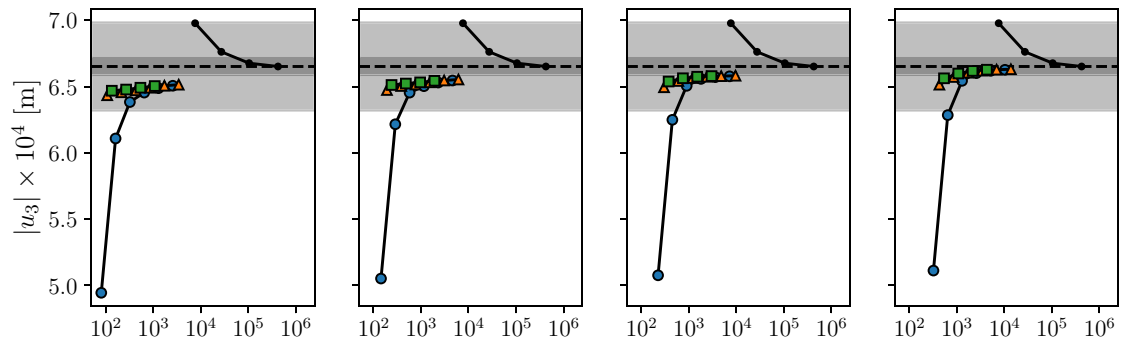
Fig. 6 Comparison between the solution obtained via a 3D FEM model and the proposed DG formulation: effect of the selected beam theory on the cross-section distribution of **a** the displacement component u_2 and **b** the stress field τ for the short beam subjected to torsion
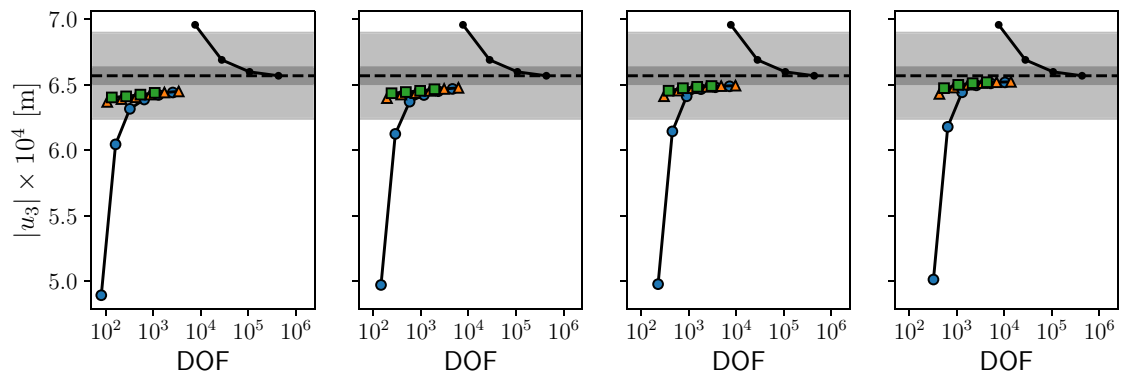
(a) One-spar beam, $L/c = 25$.

(b) Two-spar beam, $L/c = 25$.

(c) One-spar beam, $L/c = 5$.

(d) Two-spar beam, $L/c = 5$.

$$
\begin{aligned}
B_{\mathrm{IP}}(\boldsymbol{V}, \boldsymbol{U}^h) &\equiv \int_{\mathcal{D}^h} \left[\frac{\mathrm{d}\boldsymbol{V}^\intercal}{\mathrm{d}x_2} \left(\boldsymbol{Q} \frac{\mathrm{d}\boldsymbol{U}^h}{\mathrm{d}x_2} + \boldsymbol{R}\,\boldsymbol{U}^h \right) \right. \\
&\quad \left. + \boldsymbol{V}^\intercal \left(\boldsymbol{R}^\intercal \frac{\mathrm{d}\boldsymbol{U}^h}{\mathrm{d}x_2} + \boldsymbol{S}\,\boldsymbol{U}^h \right) \right] \mathrm{d}x_2 + \\
&\quad - \sum_{y \in \mathcal{I}^h} \left([\![\boldsymbol{V}]\!]^\intercal \left\{ \boldsymbol{Q}\frac{\mathrm{d}\boldsymbol{U}^h}{\mathrm{d}x_2} + \boldsymbol{R}\,\boldsymbol{U}^h \right\} \right. \\
&\quad \left. + \left\{ \frac{\mathrm{d}\boldsymbol{V}^\intercal}{\mathrm{d}x_2}\boldsymbol{Q} + \boldsymbol{V}^\intercal\boldsymbol{R}^\intercal \right\} [\![\boldsymbol{U}^h]\!] \right) + \\
&\quad - \sum_{y \in \mathcal{B}_D} \left(\nu_y \boldsymbol{V}^\intercal \left(\boldsymbol{Q}\frac{\mathrm{d}\boldsymbol{U}}{\mathrm{d}x_2} + \boldsymbol{R}\,\boldsymbol{U} \right) + \left(\frac{\mathrm{d}\boldsymbol{V}^\intercal}{\mathrm{d}x_2}\boldsymbol{Q} \right. \right. \\
&\quad \left. \left. + \boldsymbol{V}^\intercal\boldsymbol{R}^\intercal \right) \boldsymbol{U}^h \nu_y \right) + \\
&\quad + \sum_{y \in \mathcal{I}^h} \mu[\![\boldsymbol{V}]\!]^\intercal [\![\boldsymbol{U}^h]\!] + \sum_{y \in \mathcal{B}_D} \mu\boldsymbol{V}^\intercal\boldsymbol{U}^h
\end{aligned}
\tag{23}
$$

whereas the term $L_{\mathrm{IP}}(\boldsymbol{V}, \overline{\boldsymbol{B}}, \overline{\boldsymbol{T}}, \overline{\boldsymbol{U}})$ reads

$$
\begin{aligned}
L_{\mathrm{IP}}(\boldsymbol{V}, \overline{\boldsymbol{B}}, \overline{\boldsymbol{T}}, \overline{\boldsymbol{U}}) &\equiv \int_{\mathcal{D}^h} \boldsymbol{V}^\intercal \overline{\boldsymbol{B}}\, \mathrm{d}x_2 + \sum_{y \in \mathcal{B}_N} \boldsymbol{V}^\intercal \overline{\boldsymbol{T}}_y \\
&\quad - \sum_{y \in \mathcal{B}_D} \left(\frac{\mathrm{d}\boldsymbol{V}^\intercal}{\mathrm{d}x_2}\boldsymbol{Q} + \boldsymbol{V}^\intercal\boldsymbol{R}^\intercal \right) \overline{\boldsymbol{U}}_y \nu_y + \sum_{y \in \mathcal{B}_D} \mu\boldsymbol{V}^\intercal\overline{\boldsymbol{U}}_y.
\end{aligned}
\tag{24}
$$

To conclude this section, it is worth noting that the Interior Penalty formulation given in Eq. (22) verifies the Galerkin orthogonality, i.e. $B_{\mathrm{IP}}(\boldsymbol{V}, \boldsymbol{U}^h - \boldsymbol{U}) = 0$, $\forall \boldsymbol{V} \in \mathcal{V}^{hp}$, where $\boldsymbol{U}$ is the exact solution of Eqs. (14)–(16).

4 Results

The accuracy and capabilities of the formulation presented in the preceding section are assessed by investigating the effect of number of elements, selected beam theory and order of length-wise polynomial basis functions on the static response of beam structures. We employ tensor-product Legendre polynomials defined in the rectangle enclosing the cross-section of the beam as the cross-section functions appearing in Eq. (5); we use the same order of expansion for all the displacement components, i.e. $N_{u_1} = N_{u_2} = N_{u_3} = N$, and denote the corresponding N-th order beam theory by BT_N. Legendre polynomials of order p are also employed to define the space $\mathcal{V}^{hp}$ and the corresponding DG method is denoted by DG_p. Eventually, the considered beam structures

are isotropic and characterized by the Young's modulus $E = 75\,\mathrm{GPa}$ and Poisson's ratio $\nu = 0.33$.

4.1 Square Cross-section Beam

The first set of numerical tests are performed on the beam shown in Fig. 2a. The beam has a bulk square cross-section and is referred to a coordinate system located at the center of gravity of the square. The side of the cross-section is $b = 0.2\,\mathrm{m}$, whereas two different beam lengths are considered: $L/b = 100$, which represent the case of a slender beam, and $L/b = 10$, which represents the case of a relatively short beam. The beam is clamped at $x_2 = 0$ and is subjected to two different loading configurations, namely bending and torsion. As illustrated in Fig. 2a, bending is achieved by applying a force $\boldsymbol{F}_b \equiv (0, 0, -50\,\mathrm{N})^\intercal$ at $\boldsymbol{x} = (0, L, 0)^\intercal$, while torsion is achieved by applying the forces $\boldsymbol{F}_t \equiv (0, 0, 250\,\mathrm{kN})^\intercal$ and $-\boldsymbol{F}_t$ at $\boldsymbol{x} = (b/2, L, 0)^\intercal$ and $\boldsymbol{x} = (-b/2, L, 0)^\intercal$, respectively.

The magnitude of the displacement component u_3 computed at $\boldsymbol{x} = (0, L, 0)^\intercal$ for the beam subjected to bending is reported in Fig. 3 as a function of the overall number of degrees of freedom for different beam theories, different DG methods and the two considered beam lengths. In the figure, each curve corresponds to a given beam theory and DG method and is obtained by changing the number of mesh elements; more specifically, each curve contains four markers which correspond to four meshes with size $h = L/N_e$, where $N_e = 1, 2, 4$ and 8. The obtained results are compared with those provided in Ref. [9] and denoted by the thick dashed lines in Fig. 3. From the comparison, it is possible to notice that the results computed using the DG methods DG_3, DG_4 and DG_5 fall within the gray area reported in the plots, which represents the region of less than 5% deviation from the dashed line, for all the considered meshes and the considered beam theories; on the other hand, using second-order polynomial basis functions as in the DG_2 method requires a finer mesh to achieve the same level of accuracy. In fact, the numerical computations confirm that a higher order DG method provides a more accurate result than a lower order DG method using the same mesh. Eventually, as expected, changing the beam theory has as no effect on the computed values of displacement for the case of the slender beam, while it has a slightly noticeable effect for the case of the short beam.

The effect of changing the order of the beam theory or of the DG method is more evident by analyzing the distribution of the displacement and stress fields throughout the cross-section of the beam. In Figs. 4 and 5, we report the contour plots of selected components of displacement and stress fields computed using a 3D FEM code and the present DG formulation at $x_2 = L/2$ for the short beam ($L/b = 10$) subjected to bending. For each image, the contour plots are overlaid with solid black lines, which denote the contour
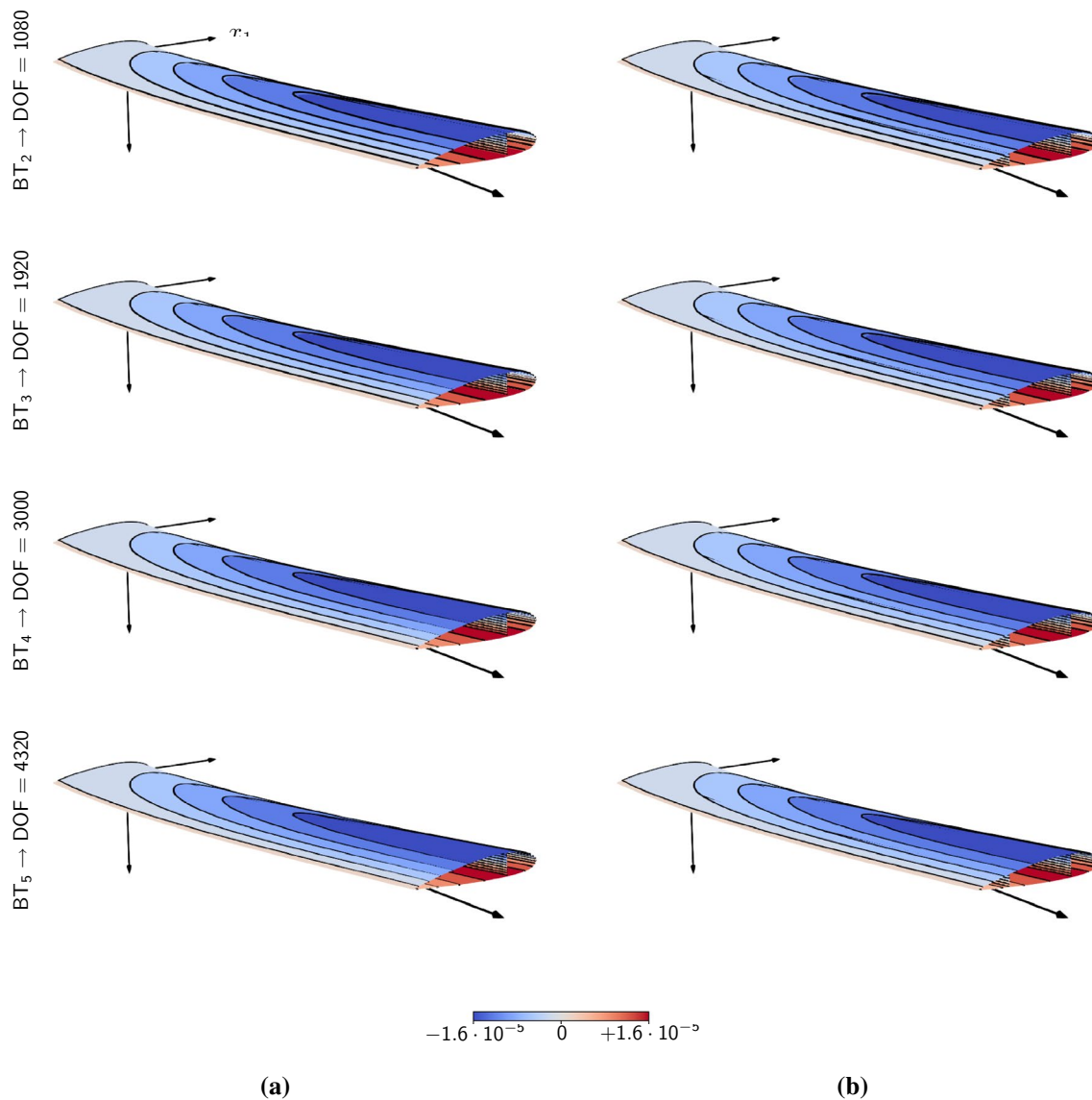
$-1.6 \cdot 10^{-5}$ 0 $+1.6 \cdot 10^{-5}$

(a)   **(b)**

Fig. 8 Comparison between the solution obtained via a shell-assembly FEM model and the proposed DG formulation: effect of the selected beam theory on the distribution of the axial component u_2 for the short beam with **a** one spar and **b** two spars subjected to bending. DG results are computed using $p = 4$ and $h = L/8$

levels obtained with the 3D FEM model with mesh size $h = b/20$ and an overall number of degrees of freedom larger than 10^6. The number of degrees of freedom DOF is also reported above each image.

The first rows of Figs. 4a, b and 5 show the displacement component u_2, the displacement component u_1 and the shear stress component σ_{23}, respectively, obtained with four successively refined finite-element meshes with mesh size $h = b/2$, $b/4$, $b/10$ and $b/20$. The same fields are computed using the BT_3 theory, the DG_2 method and four successively refined DG meshes with mesh size $h = L/4$, $L/8$, $L/16$ and $L/32$; they are reported in the second rows of Figs. 4a, b and 5. The comparison between the FEM solution and the DG

solution shows that the displacement component u_2 is well captured by both the coarsest FEM mesh (DOF = 1863) and the coarsest DG mesh (DOF = 576); the displacement component u_1 reaches convergence for the FEM model with mesh size $h = b/4$ (DOF = 10995) while the coarsest DG mesh is still able to capture it; the stress components σ_{23} reaches convergence for the FEM model with mesh size $h = b/10$ (DOF = 139623), whereas the DG model appears to require a finer mesh than $h = L/32$ (DOF = 4608) to fully recover it. The third row of Fig. 5 shows the contour plot of the σ_{23} computed using the BT_3 theory, a DG mesh size $h = L/8$ and four different DG methods; from the figures, it is possible to see that the numerical solution reaches convergence
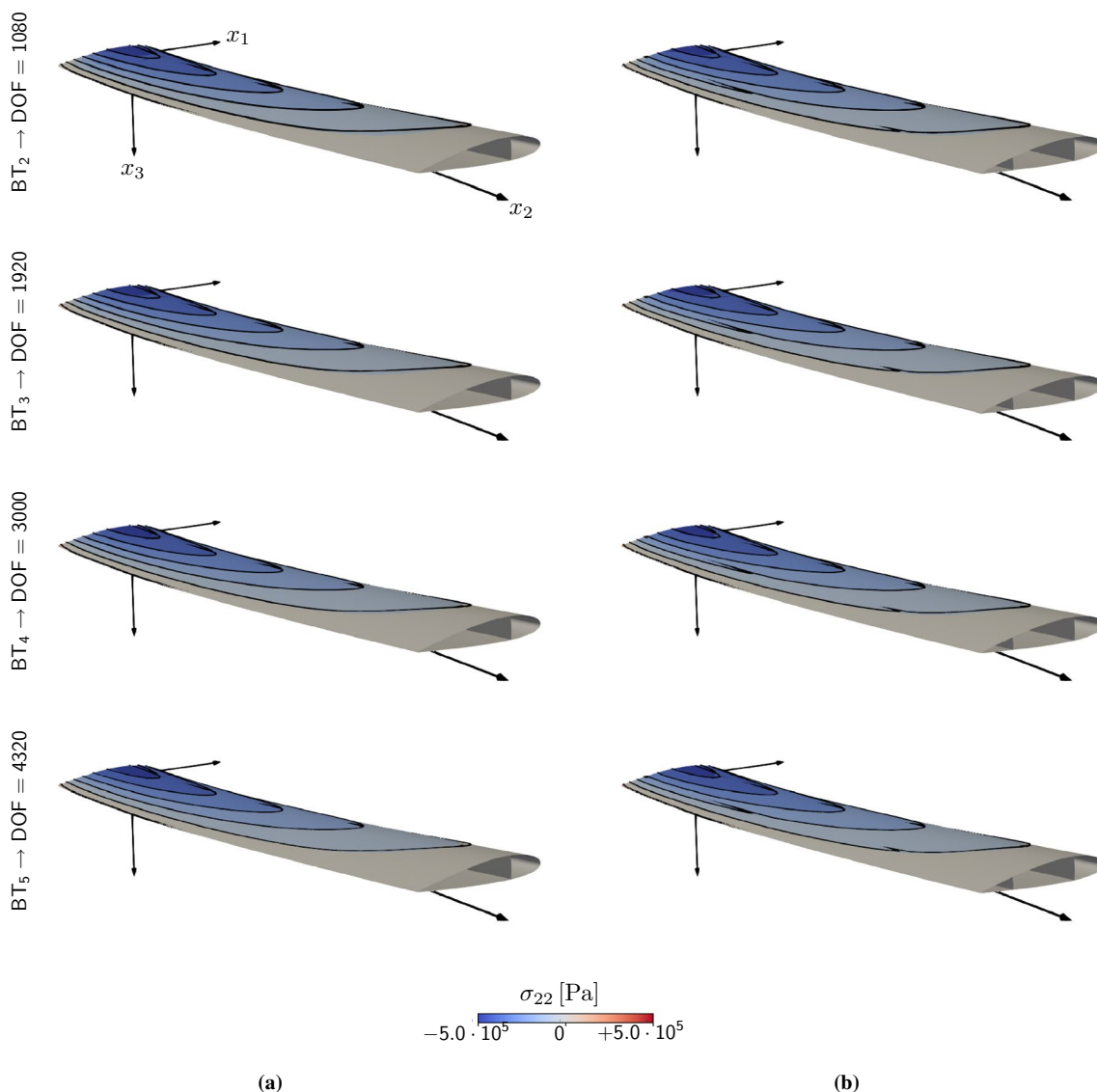
σ_{22} [Pa]

$-5.0 \cdot 10^5$ 0 $+5.0 \cdot 10^5$

(a)

(b)

Fig. 9 Comparison between the solution obtained via a shell-assembly FEM model and the proposed DG formulation: effect of the selected beam theory on the distribution of the stress component σ_{22} for the short beam with **a** one spar and **b** two spars subjected to bending. DG results are computed using $p = 4$ and $h = L/8$

Table 1 Effect of the selected beam theory on the displacement $|u_3|$ at $x = (c/4, L, 0)^{\mathsf{T}}$ for the short beam with two spars subjected to aerodynamic loading

	BT_2	BT_3	BT_4
Ref	8.5285	8.6607	8.6854
Present	8.7913	8.8488	8.8949
Error [%]	3.0814	2.1719	2.4121

Reference values are taken from Ref. [17] while the present results are obtained using the DG_4 method and a mesh size $h = L/8$

with the DG_3 method (DOF = 1536) but continues to show discrepancies with respect to the 3D FEM solution even with

the DG_5 method (DOF = 2304). This is due to the low order of the beam theory; in fact, as shown in the fourth row of Fig. 5, increasing the order of the beam theory is required to converge to the 3D FEM solution.

A similar analysis is performed for the short beam subjected to torsional loads. The comparison between the 3D FEM solution and the DG solution is reported in Figs. 6a and b for the displacement component u_2 and the shear stress $\tau \equiv \sqrt{\sigma_{13}^2 + \sigma_{23}^2}$, respectively, computed at $x_2 = L/2$. Also in this case, the contour plots are overlaid with solid black lines, which denote the contour levels obtained with the finest 3D FEM model. As shown in Fig. 6, the 3D finite-element model provides convergence for u_2 and τ with a mesh
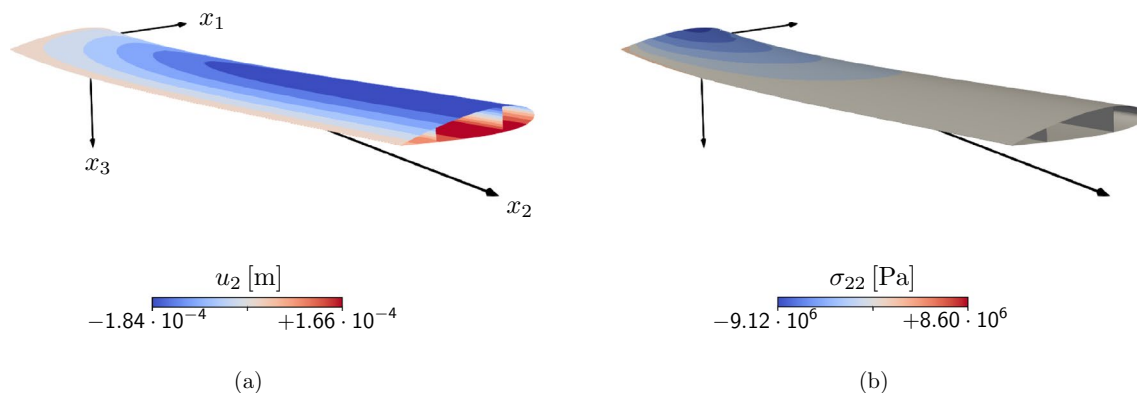
$u_2 \, [\mathrm{m}]$

$-1.84 \cdot 10^{-4} \qquad +1.66 \cdot 10^{-4}$

(a)

$\sigma_{22} \, [\mathrm{Pa}]$

$-9.12 \cdot 10^{6} \qquad +8.60 \cdot 10^{6}$

(b)

Fig. 10 **a** Displacement component u_2 and **b** stress component σ_{22} for the short beam with two spars subjected to aerodynamic loads computed using the BT_4 theory, the DG_4 method and a mesh size $h = L/8$

characterized by size $h = b/10$ and $\mathrm{DOF} = 139623$, whereas the proposed formulation fully recovers the 3D solution using the BT_5 theory, the DG_4 method and mesh size $h = L/8$, which ultimately consist of a system of 4320 degrees of freedom.

4.2 Airfoil Cross-section Beam

The second set of tests are performed on the beam displayed in Fig. 2b. The beam has a thin-walled, airfoil-shaped cross-section and is referred to a coordinate system located at one quarter of the airfoil chord. The cross-section consists of a skin, whose profile is the profile of the NACA 2415 airfoil, and two spars placed at one quarter and three quarters of the chord, i.e. at $x_1 = 0$ and $x_1 = -c/2$, respectively. Referring to the inset of Fig. 2b, the chord of the airfoil is $c = 1 \, \mathrm{m}$, the skin has thickness $\zeta_s/c = 0.006$, the spar placed at one quarter of the chord has thickness $\zeta_1/c = 0.015$, and the spar placed at three quarters of the chord has thickness $\zeta_2/c = 0.0105$. The beam is clamped at $x_2 = 0$ and is subjected to two loading conditions: either a concentrated force $\boldsymbol{F}_b \equiv (0, 0, -50 \, \mathrm{N})^{\mathsf{T}}$ applied at $\boldsymbol{x} = (0, L, 0)^{\mathsf{T}}$ or a set of aerodynamic forces $\boldsymbol{F}_a$ computed using the Vortex Lattice Methom (VLM) [41], i.e. as the result of a vortex-lattice simulation of potential flow around a flat plate occupying the surface defined by the chords of the airfoil cross-sections.

For the concentrated force loading case, four different beam configurations are considered: a slender beam having $L/c = 25$ and only the spar at $x_1 = 0$, a slender beam having $L/c = 25$ and both spars, a short beam having $L/c = 5$ and only the spar at $x_1 = 0$, and a short beam having $L/c = 5$ and both spars. The displacement component u_3 computed at $\boldsymbol{x} = (c/4, L, 0)^{\mathsf{T}}$ is shown in Fig. 7 as a function of the number of degrees of freedom for different beam theories, different DG methods and the considered beam configurations. Similar to the convergence results reported in Fig. 3, each curve corresponds to a given beam theory and DG method and is obtained by changing the number of mesh elements: the results corresponding to the DG_2 and DG_3 methods are computed using mesh size $h = L/N_e$ where $N_e = 1, 2, 4, 8, 16$ and 32, whereas the results corresponding to the DG_4 method are computed using mesh size $h = L/N_e$ where $N_e = 1, 2, 4, 8$. Figure 7 also shows the results obtained using four successively refined FEM models with mesh size $h = c/10, c/20, c/40$, and $c/80$; in this case the FEM model consists an assembly of shell regions. The comparison between the results obtained with the FEM models and the present DG formulation shows that the DG formulation reaches convergence using two to three orders of magnitude of degrees of freedom less than reference FEM model. Moreover, as expected, the first and the second rows of Fig. 3 show that varying the order of the beam theory has very little effect on the results computed for slender beams; on the other hand, a fifth-order beam theory is required to ensure that the converged DG solution fall within the dark gray area, which corresponds to the region of less than 1% deviation from the solution obtained via the most refined FEM model. Nevertheless, all solutions obtained with the DG_3 and DG_4 methods fall within the light gray area, i.e. the region of less than 5% deviation from the reference FEM solution, even using the coarsest mesh, whereas the solution obtained using the DG_2 method requires more elements to convergence.

The contour plots of the displacement component u_2 for the short beams subjected to the concentrated force are displayed in Fig. 8a, for the one-spar configuration, and in Fig. 8b, for the two-spar configuration. The first, second, third and fourth row of the figure show the results computed using the beam theories BT_2, BT_3, BT_4 and BT_5, respectively, while keeping $p = 4$ in the DG formulation

and $h = L/8$ as mesh size. The plots are reported over the deformed beam configuration and are overlaid with solid black lines, which denote the contour levels obtained via the finest FEM model. The comparison between the solution obtained via the DG method and the solution obtained via FEM shows that small differences are noticeable between the two methods when the beam theories BT_2 or BT_3 are employed, whereas the solution obtained using the beam theories BT_4 or BT_5 matches excellently the reference FEM solution. A similar observation can be made for contour plots of the stress component σ_{22}, which are displayed in Fig. 9 for the same beam configurations, DG method, mesh size and beam theory of Fig. 8. Also in this case, all beam theories well reproduce the distribution of σ_{22} with the beam theory BT_5 providing the best matching with the reference FEM model.

The last set of results focuses on the response of a wing, modeled by the present DG formulation as a beam, subjected to aerodynamic loads. These loads are computed using the VLM, which is based on replacing a lifting surface by a collection of elemental solutions, such as horseshoe or ring vortices, of the potential flow equation, and is valid for low-speed, high-Reynolds attached flow conditions [41]. The coupling between the present DG formulation and the VLM goes beyond the scope of this paper but it will be comprehensively discussed in a future study. Here, we reproduce one of the tests reported in Ref. [17], where the short beam ($L/c = 5$) with two spars is exposed to a free-stream velocity $V_\infty = 50 \, \text{m/s}$ with an angle of attack $\alpha = 3°$ at standard sea-level conditions. Unlike the preceding tests, note that the Young's modulus of the beam is $E = 69 \, \text{GPa}$. Regarding the employed VLM, the surface of the chords of the airfoil cross-sections is chosen as the lifting surface, which is discretized using an aerodynamic mesh grid of 4 ring vortices along the chord and 40 ring vortices along the length of the beam; the symmetry condition with respect to the x_1-x_3 plane is also considered for the aerodynamic computations.

The displacement component u_3 of the leading edge of the tip cross-section is computed using the DG_4 method and a mesh size $h = L/8$ and is reported in Table. 1 as a function of the selected beam theory. The table also reports the solution obtained in Ref. [17] where the authors also employed various higher order beam theories but used the FEM to solve the corresponding equations. The comparison between the solution computed using the present DG formulation and the solution obtained via FEM shows that the maximum error does not exceed 3.1% and confirms the accuracy of the proposed approach. Eventually, Fig. 10a and b show the contour plots of the displacement component u_2 and the stress component σ_{22}, respectively, obtained with the present approach using the BT_4 theory, the DG_4 method and a mesh size $h = L/8$.

5 Conclusions

A novel tool for the elastic analysis of beam structures with general cross-sections has been presented. The proposed method is based on the combined use of high-order beam theories to express the displacement components throughout the beam cross-section and high-order discontinuous Galerkin methods along the length of the beam. The accuracy of the method has been assessed by modeling cantilever beams with a square cross-section and by modeling cantilever beams with thin-walled airfoil-shaped cross-sections. Bending, torsional and aerodynamic loading cases have been considered. The obtained numerical results shows that the proposed tool is able to recover three-dimensional displacement and stress distributions using considerably fewer degrees of freedom than standard FEM approaches based on three-dimensional or two-dimensional shell elements.

Declarations

Conflict of interest On behalf of all authors, the corresponding author states that there is no conflict of interest.

References

1. Reddy, J.N.: Energy principles and variational methods in applied mechanics. John Wiley & Sons (2017)
2. Levinson, M.: A new rectangular beam theory. J. Sound Vib. **74**(1), 81–87 (1981)
3. Heyliger, P., Reddy, J.: A higher order beam finite element for bending and vibration problems. J. Sound Vib. **126**(2), 309–326 (1988)
4. Reddy, J.: On locking-free shear deformable beam finite elements. Comput. Methods Appl. Mech. Eng. **149**(1–4), 113–132 (1997). https://doi.org/10.1016/S0045-7825(97)00075-3
5. Kim, C., White, S.R.: Thick-walled composite beam theory including 3-D elastic effects and torsional warping. Int. J. Solids

Struct. **34**(31–32), 4237–4259 (1997). https://doi.org/10.1016/S0020-7683(96)00072-8

6. Taufik, A., Barrau, J.J., Lorin, F.: Composite beam analysis with arbitrary cross section. Compos. Struct. **44**(2–3), 189–194 (1999). https://doi.org/10.1016/S0263-8223(98)00134-2

7. Mistou, S., Karama, M., Lorrain, B., Faye, J.: Analysis of sandwich composite beams with a new transverse shear stress continuity model. J. Sandw. Struct. Mater. **1**(2), 96–110 (1999)

8. Karama, M., Afaq, K., Mistou, S.: Mechanical behaviour of laminated composite beam by the new multi-layered laminated composite structures model with transverse shear stress continuity. Int. J. Solids Struct. **40**(6), 1525–1546 (2003)

9. Carrera, E., Giunta, G., Nali, P., Petrolo, M.: Refined beam elements with arbitrary cross-section geometries. Comput. Struct. **88**(5–6), 283–293 (2010). https://doi.org/10.1016/j.compstruc.2009.11.002

10. Carrera, E., Petrolo, M.: On the effectiveness of higher-order terms in refined beam theories. J. Appl. Mech. (2011). https://doi.org/10.1115/1.4002207

11. Pagani, A., Yan, Y., Carrera, E.: Exact solutions for static analysis of laminated, box and sandwich beams by refined layer-wise theory. Compos. Part B Eng. **131**, 62–75 (2017)

12. Pagani, A., Carrera, E.: Large-deflection and post-buckling analyses of laminated composite beams by Carrera unified formulation. Compos. Struct. **170**, 40–52 (2017)

13. Pagani, A., Carrera, E.: Unified formulation of geometrically nonlinear refined beam theories. Mech. Adv. Mater. Struct. **25**(1), 15–31 (2018)

14. Ojo, S.O., Weaver, P.: A generalized nonlinear strong unified formulation for large deflection analysis of composite beam structures. In: AIAA Scitech 2021 Forum, page 0698. https://doi.org/10.2514/6.2021-0698 (2021)

15. Carrera, E., Petrolo, M., Nali, P.: Unified formulation applied to free vibrations finite element analysis of beams with arbitrary section. Shock Vib. **18**(3), 485–502 (2011). https://doi.org/10.3233/SAV-2010-0528

16. Carrera, E., Pagani, A., Banerjee, J.: Linearized buckling analysis of isotropic and composite beam-columns by carrera unified formulation and dynamic stiffness method. Mech. Adv. Mater. Struct. **23**(9), 1092–1103 (2016)

17. Varello, A., Carrera, E., Demasi, L.: Vortex lattice method coupled with advanced one-dimensional structural models. J. Aeroelasticity Struct. Dyn. **2**(2) (2011)

18. Grifò, M., Da Ronch, A., Benedetti, I.: A computational aeroelastic framework based on high-order structural models and high-fidelity aerodynamics. Aerosp. Sci. Technol. **132**, 108069 (2023)

19. Carrera, E., Pagani, A., Augello, R.: Large deflection of composite beams by finite elements with node-dependent kinematics. Comput. Mech. **69**(6), 1481–1500 (2022)

20. Yan, Y., Liu, B., Xing, Y., Carrera, E., Pagani, A.: Free vibration analysis of variable stiffness composite laminated beams and plates by novel hierarchical differential quadrature finite elements. Compos. Struct. **274**, 114364 (2021)

21. Le, C.I., Le, N.A.T., Nguyen, D.K.: Free vibration and buckling of bidirectional functionally graded sandwich beams using an enriched third-order shear deformation beam element. Compos. Struct. **261**, 113309 (2021)

22. Tran, T.T., Nguyen, N.H., Do, T.V., Minh, P.V., Duc, N.D.: Bending and thermal buckling of unsymmetric functionally graded sandwich beams in high-temperature environment based on a new third-order shear deformation theory. J. Sandw. Struct. Mater. **23**(3), 906–930 (2021)

23. Azzara, R., Filippi, M., Pagani, A.: Variable-kinematic finite beam elements for geometrically nonlinear dynamic analyses. Mech. Adv. Mater. Struct. 1–9 (2022)

24. Filippi, M., Pagani, A., Carrera, E.: High-order finite beam elements for propagation analyses of arbitrary-shaped one-dimensional waveguides. Mech. Adv. Mater. Struct. **29**(13), 1883–1891 (2022)

25. Jain, M., Kapuria, S.: Time-domain spectral finite element based on third-order theory for efficient modelling of guided wave propagation in beams and panels. Acta Mechanica **233**(3), 1187–1212 (2022)

26. Arnold, D.N., Brezzi, F., Cockburn, B., Marini, L.D.: Unified analysis of discontinuous Galerkin methods for elliptic problems. SIAM J. Numer. Anal. **39**(5), 1749–1779 (2002). https://doi.org/10.1137/S0036142901384162

27. Celiker, F., Cockburn, B.: Element-by-element post-processing of discontinuous galerkin methods for timoshenko beams. J. Sci. Comput. **27**, 177–187 (2006)

28. Celiker, F., Cockburn, B., Stolarski, H.K.: Locking-free optimal discontinuous Galerkin methods for Timoshenko beams. SIAM J. Numer. Anal. **44**(6), 2297–2325 (2006)

29. Eptaimeros, K., Koutsoumaris, C.C., Tsamasphyros, G.: Interior penalty discontinuous Galerkin FEMs for a gradient beam and CNTs. Appl. Numer. Math. **144**, 118–139 (2019). https://doi.org/10.1016/j.apnum.2019.05.020

30. Becker, G., Noels, L.: A fracture framework for Euler-Bernoulli beams based on a full discontinuous Galerkin formulation/extrinsic cohesive law combination. Int. J. Numer. Methods Eng. **85**(10), 1227–1251 (2011)

31. Gulizzi, V., Benedetti, I., Milazzo, A.: An implicit mesh discontinuous Galerkin formulation for higher-order plate theories. Mech. Adv. Mater. Struct. **27**(17), 1494–1508 (2020). https://doi.org/10.1080/15376494.2018.1516258

32. Gulizzi, V., Benedetti, I., Milazzo, A.: A high-resolution layerwise discontinuous Galerkin formulation for multilayered composite plates. Compos. Struct. **242**, 112137 (2020). https://doi.org/10.1016/j.compstruct.2020.112137

33. Guarino, G., Milazzo, A., Gulizzi, V.: Equivalent-Single-Layer discontinuous Galerkin methods for static analysis of multilayered shells. Appl. Math. Model. **98**, 701–721 (2021). https://doi.org/10.1016/j.apm.2021.05.024

34. Guarino, G., Gulizzi, V., Milazzo, A.: High-fidelity analysis of multilayered shells with cut-outs via the discontinuous Galerkin method. Compos. Struct. **276**, 114499 (2021). https://doi.org/10.1016/j.compstruct.2021.114499

35. Benedetti, I., Gulizzi, V., Milazzo, A.: Layer-Wise discontinuous Galerkin methods for piezoelectric laminates. Modelling **1**(2), 198–214 (2020). https://doi.org/10.3390/modelling1020012

36. Guarino, G., Milazzo, A.: A discontinuous galerkin formulation for nonlinear analysis of multilayered shells refined theories. Int. J. Mech. Sci. **255**, 108426 (2023)

37. Guarino, G., Gulizzi, V., Milazzo, A.: Accurate multilayered shell buckling analysis via the implicit-mesh discontinuous Galerkin method. AIAA J. **60**(12), 6854–6868 (2022). https://doi.org/10.2514/1.J061933

38. Jones, R.M.: Mechanics of composite materials. CRC Press (2018). ISBN 156032712X

39. Gulizzi, V., Almgren, A.S., Bell, J.B.: A coupled discontinuous galerkin-finite volume framework for solving gas dynamics over embedded geometries. J. Comput. Phys. **450**, 110861 (2022)

40. Gulizzi, V., Saye, R.: Modeling wave propagation in elastic solids via high-order accurate implicit-mesh discontinuous galerkin methods. Comput. Methods Appl. Mech. Eng. **395**, 114971 (2022)

41. Bertin, J.J., Cummings, R.M.: Aerodynamics for engineers. Cambridge University Press (2021). ISBN 1009115758